The Astrophysical Journal Letters, 843:L36 (6pp), 2017 July 10 https://doi.org/10.3847/2041-8213/aa7cfe

Abundant Methanol Ice toward a Massive Young Stellar Object in the Central Molecular Zone*

Deokkeun An[1,7], Kris Sellgren[2,7], A. C. Adwin Boogert[3], Solange V. Ramírez[4], and Tae-Soo Pyo[5,6]
[1] Department of Science Education, Ewha Womans University, 52 Ewhayeodae-gil, Seodaemun-gu, Seoul 03760, Korea; deokkeun@ewha.ac.kr
[2] Department of Astronomy, Ohio State University, 140 West 18th Avenue, Columbus, OH 43210, USA
[3] Universities Space Research Association, Stratospheric Observatory for Infrared Astronomy, NASA Ames Research Center, MS 232-11, Moffett Field, CA 94035, USA
[4] NASA Exoplanet Science Institute, California Institute of Technology, Mail Stop 100-22, Pasadena, CA 91125, USA
[5] Subaru Telescope, National Astronomical Observatory of Japan, National Institutes of Natural Sciences (NINS), 650 North A'ohoku Place, Hilo, HI 96720, USA
[6] School of Mathematical and Physical Science, SOKENDAI (The Graduate University for Advanced Studies), Hayama, Kanagawa 240-0193, Japan
Received 2017 May 23; revised 2017 June 23; accepted 2017 June 29; published 2017 July 13

Abstract

Previous radio observations revealed widespread gas-phase methanol (CH_3OH) in the Central Molecular Zone (CMZ) at the Galactic center (GC), but its origin remains unclear. Here, we report the discovery of CH_3OH ice toward a star in the CMZ, based on a Subaru 3.4–4.0 μm spectrum, aided by NASA/IRTF L' imaging and 2–4 μm spectra. The star lies ∼8000 au away in projection from a massive young stellar object (MYSO). Its observed high CH_3OH ice abundance (17% ± 3% relative to H_2O ice) suggests that the 3.535 μm CH_3OH ice absorption likely arises in the MYSO's extended envelope. However, it is also possible that CH_3OH ice forms with a higher abundance in dense clouds within the CMZ, compared to within the disk. Either way, our result implies that gas-phase CH_3OH in the CMZ can be largely produced by desorption from icy grains. The high solid CH_3OH abundance confirms the prominent 15.4 μm shoulder absorption observed toward GC MYSOs arises from CO_2 ice mixed with CH_3OH.

Key words: astrochemistry – Galaxy: nucleus – ISM: abundances – stars: massive – stars: protostars

1. Introduction

Methanol (CH_3OH) is a key species in the formation of complex organic molecules. CH_3OH is observed in gas phase throughout the Central Molecular Zone (CMZ), the innermost ∼400 pc region of the Milky Way (see Morris & Serabyn 1996), with a wide variation in abundance relative to H_2 (∼10^{-8}–10^{-6}; Requena-Torres et al. 2006; Yusef-Zadeh et al. 2013). Complex organic molecules are also observed throughout the CMZ, with high and constant gas-phase abundances, relative to gas-phase CH_3OH, that are matched by hot cores in the Galactic disk (Requena-Torres et al. 2006).

Gas-phase production of CH_3OH is inefficient, but formation by the hydrogenation of CO ices in dense (∼10^5 cm^{-3}) and cold (∼15 K) environments, such as dense molecular cores, is very active as shown by laboratory experiments and Monte Carlo simulations (e.g., Watanabe et al. 2003; Cuppen et al. 2009; Coutens et al. 2017). A number of non-thermal desorption mechanisms, including shocks (Requena-Torres et al. 2008), cosmic rays (Yusef-Zadeh et al. 2013), and episodic explosions (Coutens et al. 2017) have been proposed to explain the widespread gas-phase CH_3OH (possibly along with other complex molecules; see Rawlings et al. 2013) in the CMZ. However, previous searches for CH_3OH ice in the CMZ have been unsuccessful; only upper limits on the abundance of solid CH_3OH relative to H_2O ice, $N_{solid}(CH_3OH)/N_{solid}(H_2O)$, have been established from Sgr A* (<0.04) and the Quintuplet cluster star GCS 3-I (<0.27) (Chiar et al. 2000; Gibb et al. 2004; Moultaka et al. 2015).

Indirect evidence of the presence of solid CH_3OH came from mid-infrared spectra of massive young stellar objects (MYSOs) in the Galactic center (GC) region (An et al. 2009, 2011). We identified these GC MYSOs by their wide absorption profile of 15 μm CO_2 ice, with a strong "shoulder" absorption component centered at 15.4 μm. To date, this 15.4 μm shoulder has only been observed toward disk MYSOs (Boogert et al. 2015 and references therein). Laboratory studies attribute the 15.4 μm shoulder absorption to Lewis interaction of CO_2 in icy grains with other molecules such as methanol, ethanol, butanol, or diethylether (Dartois et al. 1999a). CH_3OH has the highest abundance of these toward Galactic disk MYSOs.

The question emerges as to whether the observed 15.4 μm shoulder CO_2 ice absorption in the CMZ is produced by Lewis-base molecules other than CH_3OH because of the unusual CMZ conditions. CMZ molecular clouds are warmer, denser, and more turbulent than molecular clouds in the disk. Stronger tidal shear forces and magnetic fields pervade the CMZ (see Morris & Serabyn 1996 and references therein). The cosmic ray ionization rate is higher than in the disk (Goto et al. 2008). All these effects may complicate and lead to chemical networks that are distinct from those under local cloud conditions.

In this letter, we report the first direct detection of solid CH_3OH in the CMZ by searching for the 3.535 μm ν_3 C–H stretching mode of CH_3OH ice in the GC MYSO SSTGC 726327. The 3.535 μm absorption is almost independent of ice mantle composition (Hudgins et al. 1993; Ehrenfreund et al. 1999), and therefore can be used to reliably measure a column density of solid CH_3OH. SSTGC 726327 is one of 35 MYSOs identified in the GC using 5–35 μm *Spitzer*/IRS spectra (An et al. 2009, 2011), with both the 15.4 μm shoulder CO_2 ice and 14.97 μm gas-phase CO_2 absorption. Its silicate feature

* Based in part on data collected at Subaru Telescope, which is operated by the National Astronomical Observatory of Japan.
[7] Visiting Astronomer at the Infrared Telescope Facility, which is operated by the University of Hawaii under contract NNH14CK55B with the National Aeronautics and Space Administration.

implies an integrated (both foreground and internal) visual extinction $A_V = 46 \pm 3$ mag, while the foreground extinction from the Galactic disk is 30 ± 4 mag (Schultheis et al. 2009).

2. Observations and Data Reductions

2.1. IRTF

We acquired L'-band images of SSTGC 726327 with NSFCAM2 (Shure et al. 1994) at the 3.0 m NASA/IRTF on 2010 July 19 (UT). We took two sets of images in a 3×3 dither pattern, yielding a total effective exposure time of 315 s for each set. The FWHM of image was 0.″5. We used standard IRAF[8] routines to reduce images and extract photometry. SSTGC 726327 is a point source in [3.6] IRAC images (Ramírez et al. 2008). Our higher-resolution L' image resolves SSTGC 726327 into faint extended emission plus two point sources separated by 2″: SSTGC 726327E (UGPS J174653.31-283201.2) and SSTGC 726327W (UGPS J174653.16-283201.5).

In addition to the L' images, we obtained a 2–4 μm spectrum of SSTGC 726327E with SpeX (Rayner et al. 2003) at the NASA/IRTF, on 2009 May 15 (UT). We observed through varying amounts of cirrus in the long cross-dispersed mode. The slit width of 0.″5, matching the seeing, resulted in $\lambda/\Delta\lambda = R \approx 1500$. We nodded the telescope along the north–south slit. The total on-source integration time was 32 minutes.

Flat field, argon arc, and telluric standard spectra were taken immediately before and after the observation. The airmass difference between the object and telluric standard spectra was negligible. The spectra were extracted using Spextool, a spectral extraction package for SpeX (Cushing et al. 2004), in the point source extraction mode. We corrected for telluric absorption following the standard procedures in Vacca et al. (2003). We flagged wavelengths with strong atmospheric absorptions from a telluric standard spectrum by taking a difference from its pseudo continuum, which was fit by a 5th-order polynomial in each spectral order. We removed data points with less than 50% atmospheric transmission. The signal-to-noise ratio (S/N) of the final spectrum is 18 at 3.6–4.0 μm.

2.2. Subaru

We obtained 3.4–4.0 μm high-resolution spectra of SSTGC 726327E and SSTGC 726327W with the echelle mode of IRCS (Kobayashi et al. 2000), combined with an adaptive optics (AO) system, at the 8.2 m Subaru telescope on 2014 June 20 (UT). The sky was mostly clear. The seeing was 0.″2 in FWHM after the AO correction. We nodded the two objects along the slit (0.″28 × 6.″69, $R \sim 10{,}000$) for sky subtraction. We used LB^-, LB^0, and LB^+ configurations to have continuous spectral coverage. The total on-source integration time for SSTGC 726327E was 3.1 hr in LB^0, which covers most of the CH_3OH ice band, and 0.7 hr each in LB^- and LB^+.

We observed a set of A-type stars every hour for wavelength, telluric, and flux calibrations. We grouped individual frames, depending on the time of observations and air masses, and made co-added echelle frames before extraction. We extracted spectra using IRAF routine apall with an extraction aperture of 0.″9. We corrected for hydrogen absorption lines in the standard star spectra using a smoothed theoretical spectrum of Vega (Castelli & Kurucz 2004)[9], and then derived telluric corrections. We flagged and removed data where the atmospheric transmission, relative to an observed psuedo continuum, was <50%. We averaged the flux into 3 nm wide bins in steps of 1.5 nm. Our final spectrum has $R \approx 600$ and S/N of 42 per binned data point in LB^0 and S/N ≈ 24 in LB^- and LB^+. The SSTGC 726327W spectrum was extremely noisy and will not be discussed further.

Our flux calibrated Subaru/IRCS spectra are fainter than IRTF/SpeX L-band spectra by almost a factor of two, and show mild flux differences (∼2%–3%) in order overlaps. To correct for this, we scaled the IRCS spectra to match our IRTF spectrum by taking a median difference in logarithmic flux at 3.6–3.9 μm for each of the three echelle configurations.

3. Results

Figure 1 compares our L' image (middle) with the K-band image from the UKIDSS Galactic Plane Survey (Lucas et al. 2008; top) and the *Spitzer*/IRAC [4.5] channel image (Ramírez et al. 2008; bottom). UKIDSS photometry plus our point-spread function fitting photometry shows that $L' = 9.3$ for SSTGC 726327E, with $H - K = 2.7$ and $K - L' = 1.6$. The L' (3.8 μm) photometry is in good agreement with [3.6] = 9.3 for SSTGC 726327 (Ramírez et al. 2008). The extended emission we detect at L', but not at K, roughly coincides with the 3″ (0.12 pc) diameter H II region Sgr B1 A (Mehringer et al. 1992, dotted circle), also known as GPSR5 0.488–0.028 (Becker et al. 1994).

The IRAC source SSTGC 726327 is a composite of flux from SSTGC 726327E, SSTGC 726327W, the H II region, and the MYSO. The IRAC position, relative to SSTGC 726327E, is 0.″9 west at 4.5 μm, but is located further away (1.″1) at 8.0 μm (Ramírez et al. 2008). Morales & Robitaille (2017) find that, when a candidate YSO selected based on *Spitzer*/IRAC photometry is matched to a UKIDSS source by their spectral energy distributions, 94% of the *Spitzer* and UKIDSS sources are separated by ⩽0.″57. This suggests SSTGC 726327 and SSTGC 726327E are distinct sources with a projected separation, for a GC distance of 8 kpc, of 6000 to 10,000 au.

The top panel in Figure 2 shows our 2–4 μm IRTF/SpeX spectrum of SSTGC 726327E (blue line). The spectrum shows photospheric 2.3 μm CO band-head absorption, demonstrating that SSTGC 726327E is probably a background giant star rather than a MYSO. The observed Br γ (2.166 μm) and Br α (4.051 μm) emission likely arise in the Sgr B1 A H II region.

We searched for the best-fitting spectral type, the peak optical depth of the 3.0 μm H_2O ice band [$\tau_{\rm solid}(H_2O)$], and foreground dust extinction of SSTGC 726327E, by utilizing the IRTF/SpeX spectral library (Rayner et al. 2009), the optical constants of 10 K amorphous H_2O ice on 0.4 μm grains, and the extinction curve derived from the line of sight to a dense core (Boogert et al. 2011). We minimized the reduced χ^2 (χ^2_ν) of the fit to the SpeX spectra and J and H UKIDSS photometry ($J = 18.391 \pm 0.068$ and $H = 13.571 \pm 0.003$). We masked Br α and Br γ emission lines, and excluded data points at 3.1 μm ⩽ λ ⩽ 3.7 μm to avoid the 3.4 μm absorption band discussed later. We multiplied the K and L spectra by a constant factor (1.16) to match the UKIDSS K-band measurement ($K = 10.915 \pm 0.003$).

[8] IRAF is distributed by the National Optical Astronomy Observatory, which is operated by the Association of Universities for Research in Astronomy (AURA) under a cooperative agreement with the National Science Foundation.

[9] http://kurucz.harvard.edu/stars/vega/

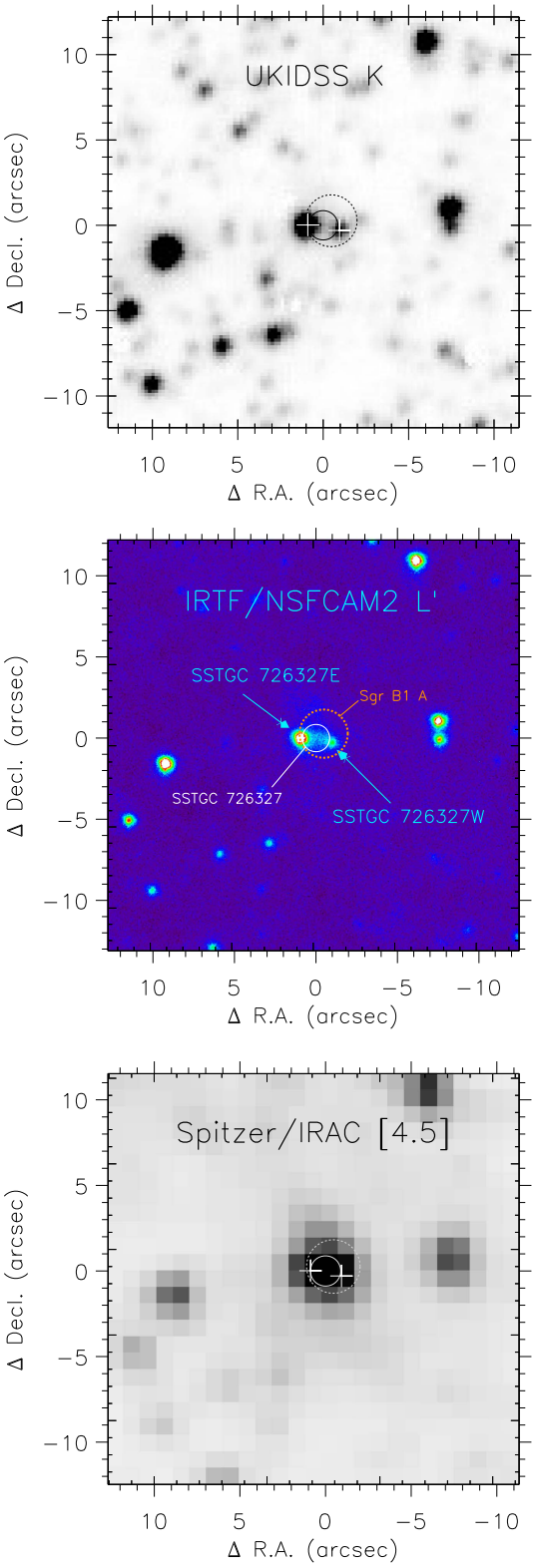

Figure 1. Near- and mid-IR images centered on SSTGC 726327. Top: *K* image from the UKIDSS Galactic Plane Survey (0.″8 resolution; Lucas et al. 2008). Middle: *L*′ image from IRTF/NSFCAM2 (0.″5 resolution; this paper). Bottom: *Spitzer*/IRAC [4.5] image (1.″7 resolution; Ramírez et al. 2008). The *L*′ image shows that the MYSO SSTGC 726327 (solid circle with 1.″7 diameter), a point source in *Spitzer*/IRAC images, is resolved into two point sources (SSTGC 726327E and SSTGC 726327W; plus symbols) plus diffuse emission. A dotted circle marks the location and diameter (3″) of the H II region Sgr B1 A (Mehringer et al. 1992). North is to the top and east is to the left.

We found that SSTGC 726327E is likely a M giant or K/M supergiant, along with $\tau_{\rm solid}(H_2O) = 1.7 \pm 0.3$ and $A_K = 4.2 \pm 0.5$. The errors represent a range of values within $\Delta\chi^2_\nu < 2$ from the minimum χ^2_ν (0.83). We found a 30% smaller A_K if we used the GC extinction curve from Fritz et al. (2011) instead; spectral types and $\tau_{\rm solid}(H_2O)$ essentially remain unchanged within the errors. The green line in the top panel of Figure 2 shows our best-fitting spectrum (M6.5 III; HD 142143) with added reddening ($A_K = 4.15$). The red line represents the best-fitting spectrum to our IRTF/SpeX data, with the 3 μm H_2O ice absorption [$\tau_{\rm solid}(H_2O) = 1.51$] added to the reddened M6.5 III spectrum. The optical depth spectrum with respect to the best-fitting model is shown in the bottom panel of Figure 2. The strong, broad 3.4 μm absorption band in SSTGC 726327E is a blend of two distinct absorption features from icy molecular cloud grains (Brooke et al. 1999) and foreground diffuse cloud dust (Sandford et al. 1991; Pendleton et al. 1994).

In the left panel of Figure 3, our 3.4–4.0 μm IRCS spectra of SSTGC 726327E are shown before ("original") and after scaling the flux to match the IRTF data ("corrected"). Methanol ice absorption is seen at 3.535 μm in our IRTF spectrum (Figure 2), but it is more clearly observed in the IRCS spectra. We do not detect the weaker CH_3OH features at 3.84 μm and 3.94 μm (Dartois et al. 1999b).

We derived a local continuum across the 3.535 μm band using a first order polynomial fitted at $3.448 \leqslant \lambda \leqslant 3.497$ μm (2860–2900 $\rm cm^{-1}$) and $3.597 \leqslant \lambda \leqslant 3.650$ μm (2740–2780 $\rm cm^{-1}$) in wavenumber space (dotted line). The right panel in Figure 3 shows the optical depth derived by dividing the "corrected" IRCS spectra by the local continuum. We employed a laboratory transmission spectrum of 10 K pure CH_3OH ice (Hudgins et al. 1993), in which the 3.535 μm band overlaps with another, wide band, centered at 3.39 μm (2960 $\rm cm^{-1}$) from the ν_9 C–H stretching mode. We fitted a first order polynomial to the laboratory spectrum over the same wavelength intervals adopted for the continuum construction, and isolated the 3.535 μm component by subtracting the local baseline. The solid lines in Figure 3 show our best-fitting model spectrum for CH_3OH ice, which has a peak optical depth at 3.535 μm, $\tau_{\rm solid}(CH_3OH)$, of 0.10 ± 0.01. This agrees with a result from an alternative approach, in which we restricted our fit to 3.45–3.64 μm and simultaneously searched for the flux scaling factors of individual IRCS orders and the best-fitting laboratory CH_3OH ice spectrum.

Table 1 summarizes the 3.535 μm CH_3OH ice optical depth and column density for SSTGC 726327E. The shape and the intrinsic integrated band strength (A) for the 3.535 μm C–H stretch mode have a weak dependence on temperature and abundance of ice mantles (e.g., Ehrenfreund et al. 1999; Kerkhof et al. 1999). We averaged values from Hudgins et al. (1993) and Schutte et al. (1996) to adopt $A = 5.95 \pm 0.65 \times 10^{-18}$ cm molecule^{-1} for CH_3OH ice, then derived its column density. We also list $\tau_{\rm solid}(H_2O)$ for SSTGC 726327E. We computed $N_{\rm solid}(H_2O)$ by multiplying $\tau_{\rm solid}(H_2O)$ by FWHM $\approx 330\,\rm cm^{-1}$, and assuming $A = 2.0 \times 10^{-16}$ cm molecule^{-1} (Hagen et al. 1981).

4. Discussion

In this letter, we present the first detection of CH_3OH ice absorption toward the CMZ, in the background star SSTGC 726327E. Geballe & Oka (2010) identified 2.27 μm

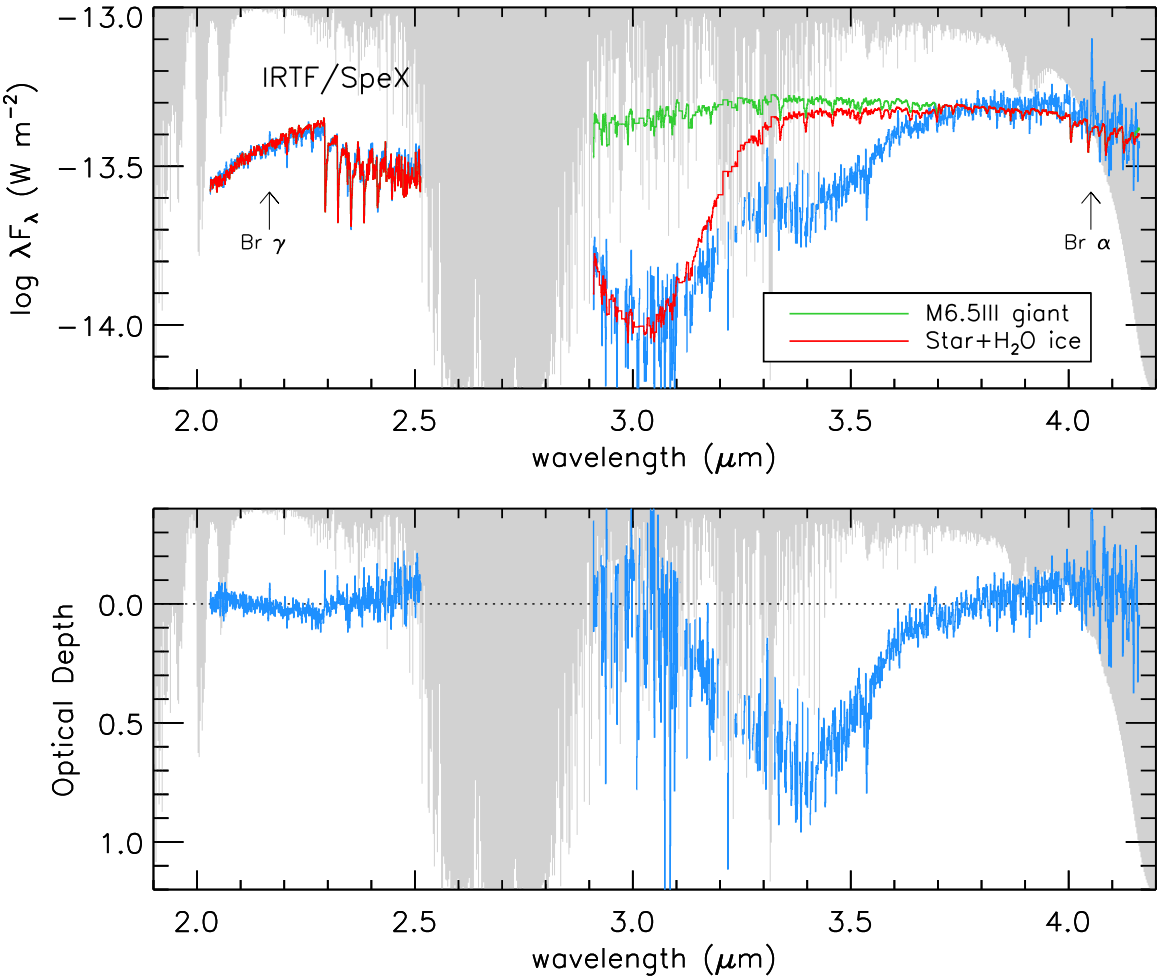

Figure 2. Top: IRTF/SpeX spectra of SSTGC 726327E (blue line). The red line shows the best-fitting spectrum of the M6.5 III star (HD 94705) in the IRTF/SpeX library (Rayner et al. 2009) with added reddening and 3.0 μm H_2O ice absorption from 0.4 μm ice grains at 10 K (Boogert et al. 2011). The green line is the same best-fitting spectrum, but without H_2O ice absorption. Bottom: optical depth spectra computed using the best-fitting model. In each panel, theoretical atmospheric transmission curves at Maunakea are shown by gray shades scaled from 0 to 1.

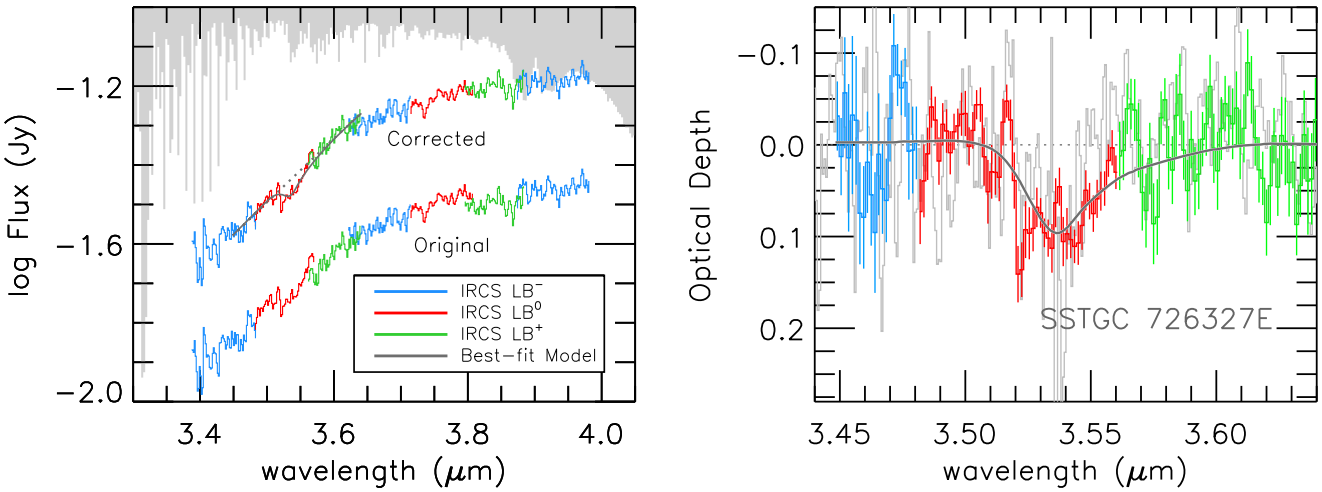

Figure 3. Left: Subaru/IRCS *L*-band spectrum of SSTGC 726327E. The "original" spectra represent those calibrated and corrected for telluric absorptions. The "corrected" spectra are the same, except that additional zero-point flux offsets are applied in each of the three IRCS configurations (blue, red, and green lines for LB^-, LB^0, and LB^+, respectively) to match our IRTF/SpeX spectrum. The dotted line is a linear fit to the continuum around the 3.535 μm CH_3OH ice band, and the solid line represents the best-fitting laboratory spectrum of pure CH_3OH ice at 10 K (Hudgins et al. 1993). Theoretical atmospheric transmission curves at Maunakea are shown by gray shade scaled from 0 to 1. Right: optical depth spectra derived from the local continuum for SSTGC 726327E and the best-fitting model spectrum. IRTF/SpeX data are shown in gray line.

Table 1
Peak Optical Depth and Column Density of Solid H_2O and CH_3OH

Object(s)	A_V	$\tau_{solid}(H_2O)$	$N_{solid}(H_2O)$	$\tau_{solid}(CH_3OH)$	$N_{solid}(CH_3OH)$	$N_{solid}(CH_3OH)/N_{solid}(H_2O)$
	(mag)		(10^{18} cm^{-2})		(10^{18} cm^{-2})	
SSTGC 726327E	24–43[a]	1.7 ± 0.3	2.8 ± 0.5	0.10 ± 0.01	0.47 ± 0.05	0.17 ± 0.03
Sgr A*	30	0.50 ± 0.01	1.24 ± 0.25	<0.01	<0.05	<0.04
GCS 3 I	29	0.23 ± 0.02	0.47 ± 0.04	<0.03	<0.13	<0.27
Massive YSOs						<0.03–0.31
Low-mass YSOs						<0.01–0.25
Quiescent clouds						<0.01–0.12

Note. References for the Galactic center sources: SSTGC 726327E (this paper); Sgr A* and GCS 3-I (Chiar et al. 2000; Gibb et al. 2004). Minimum and maximum values for source classes from Boogert et al. (2015).
[a] A range bracketed by values from our model fitting, either $A_K = 4.2 \pm 0.5$ with a dense core extinction curve (Boogert et al. 2011) or a 30% lower A_K from model fitting with a GC extinction law (Fritz et al. 2011). We assumed $A_K/A_V = 0.11$.

absorption in a background GC star as possibly due to CH_3OH ice, but the absence of 3.53 μm CH_3OH ice absorption rules out this identification (T. R. Geballe, 2016, private communication). Table 1 compares $N_{solid}(CH_3OH)/N_{solid}(H_2O) = 0.17 \pm 0.03$ toward SSTGC 726327E to previous upper limits from a $14'' \times 20''$ aperture placed on Sgr A* and from the Quintuplet cluster star GCS 3-I (Chiar et al. 2000; Gibb et al. 2004). $N_{solid}(CH_3OH)/N_{solid}(H_2O)$ is $\gtrsim$4 times higher toward SSTGC 726327E than toward Sgr A*.

SSTGC 726327E is ~8000 au in projection from the MYSO SSTGC 726327 in Sgr B1. The CH_3OH ice absorption we detect toward SSTGC 726327E likely arises from the extended envelope of the MYSO, which can extend to ~30,000–90,000 au (e.g., van der Tak et al. 2000b). Pontoppidan et al. (2004) have measured column densities of CH_3OH ice from an extended envelope of a low-mass Class 0 protostar, Serpens SMM 4, based on the *L*-band spectra of 10 pre-main sequence stars. These "background" stars show a constant $N_{solid}(CH_3OH)/N_{solid}(H_2O) \sim 0.3$ at projected distances of 4000–10,000 au from Serpens SMM 4, then no CH_3OH at a projected distance of 19,000 au. They conclude, as we do, that some or all CH_3OH ice absorption arises from the extended envelope of the YSO.

While we have discovered CH_3OH ice in one line of sight to CMZ, CH_3OH ice is found in abundance not only in YSOs, but also toward stars behind cold, quiescent molecular clouds and cores in the Galactic disk at $A_V \gtrsim 9$ mag (Table 1; Boogert et al. 2015). For two disk MYSOs (RAFGL 7009S and W33 A; Brooke et al. 1999; Dartois et al. 1999b), $N_{solid}(CH_3OH)/N_{solid}(H_2O)$ is higher than the maximum value observed toward stars behind quiescent cores in the disk (0.12; Boogert et al. 2011). This empirical division also makes the case for SSTGC 726327E being behind the envelope of the MYSO SSTGC 726327.

If SSTGC 726327 has physical and chemical structures similar to those of W33 A (van der Tak et al. 2000a, 2000b), the maximum gas density encountered along the line of sight at the projected distance of 8000 au is $\sim 6 \times 10^5$ cm^{-3}, which is sufficiently large enough to maintain CH_3OH formation in its envelope. However, the gas temperature within the MYSO envelope likely exceeds the sublimation temperature of CO (~20 K) all the way to the edge of the MYSO, under which additional growth of CH_3OH on ice mantles should be suppressed (Watanabe et al. 2003; Cuppen et al. 2009). CMZ clouds are on average warmer than in the disk, but there are dense shielded regions with cold (~15 K) dust grains (Rodríguez-Fernández et al. 2004; Molinari et al. 2011), where CH_3OH can form. Then it is possible that CH_3OH ice grains arise in dense molecular clouds within the CMZ, in which case the star SSTGC 726327E is projected by chance next to the MYSO.

The fractional abundance of CH_3OH ice with respect to H_2 is $\sim 10^{-5}$ toward SSTGC 726327E, if our best-fitting A_K is taken with $A_K/A_V = 0.11$ and $N(H_2)/A_V \sim 10^{21}$ cm^{-2} mag^{-1} (see Hasenberger et al. 2016, and references therein). This order of magnitude estimate is $\sim 10^1$–10^3 times larger than the gas-phase CH_3OH abundance in the CMZ (Requena-Torres et al. 2006; Yusef-Zadeh et al. 2013). While systematic searches for CH_3OH ices should be proceeded before making any firm conclusions, our estimate suggests that gas-phase CH_3OH in the CMZ can be largely produced by desorption of CH_3OH from icy grains (e.g., Requena-Torres et al. 2008; Yusef-Zadeh et al. 2013; Coutens et al. 2017).

In spite of abundant CH_3OH ices in various sight lines, broad CO_2 ice bands with the 15.4 μm shoulder absorption have, to date, only been observed toward YSOs (Boogert et al. 2015). About 19% of the CO_2 absorption in SSTGC 726327 is attributed to the shoulder CO_2 (An et al. 2011). With our measurement of CH_3OH abundance, we found $N_{solid}(CH_3OH)/N_{solid}(CO_2$ shoulder$) = 3.9 \pm 0.4$. We applied the same spectral decomposition procedure to the observed CO_2 ice profile of the ISO spectrum of W33 A (Gerakines et al. 1999), and found 10% for the fraction of the shoulder component, which results in $N_{solid}(CH_3OH)/N_{solid}(CO_2$ shoulder$) = 11.2 \pm 2.4$ based on $N_{solid}(CH_3OH)$ in Brooke et al. (1999). Although there exists a factor of three difference in this comparison, systematic errors likely dominate, since our measurement only traces CH_3OH ice in the outer part of the MYSO. The similar $N_{solid}(CH_3OH)/N_{solid}(CO_2$ shoulder$)$ implies that CH_3OH is indeed the best candidate for interacting molecules in the observed 15.4 μm shoulder CO_2 toward GC MYSOs (An et al. 2009, 2011), as it is in disk MYSOs. Additional observations are clearly needed to extend a source list, establish their properties, and estimate the variance of CH_3OH ice in the CMZ.

D.A. acknowledges support provided by Basic Science Research Program through the National Research Foundation of Korea (NRF) funded by the Ministry of Education (NRF-2015R1D1A1A09058700) and by the Korean NRF to the Center for Galaxy Evolution Research (No. 2010-0027910).

Facilities: IRTF, Subaru.

References

An, D., Ramírez, S. V., Sellgren, K., et al. 2009, ApJL, 702, L128
An, D., Ramírez, S. V., Sellgren, K., et al. 2011, ApJ, 736, 133
Becker, R. H., White, R. L., Helfand, D. J., & Zoonematkermani, S. 1994, ApJS, 91, 347
Boogert, A. C. A., Gerakines, P. A., & Whittet, D. C. B. 2015, ARA&A, 53, 541
Boogert, A. C. A., Huard, T. L., Cook, A. M., et al. 2011, ApJ, 729, 92
Brooke, T. Y., Sellgren, K., & Geballe, T. R. 1999, ApJ, 517, 883
Castelli, F., & Kurucz, R. L. 2004, arXiv:astro-ph/0405087
Chiar, J. E., Tielens, A. G. G. M., Whittet, D. C. B., et al. 2000, ApJ, 537, 749
Coutens, A., Rawlings, J. M. C., Viti, S., & Williams, D. A. 2017, MNRAS, 467, 737
Cuppen, H. M., van Dishoeck, E. F., Herbst, E., & Tielens, A. G. G. M. 2009, A&A, 508, 275
Cushing, M. C., Vacca, W. D., & Rayner, J. T. 2004, PASP, 116, 362
Dartois, E., Demyk, K., d'Hendecourt, L., & Ehrenfreund, P. 1999a, A&A, 351, 1066
Dartois, E., Schutte, W., Geballe, T. R., et al. 1999b, A&A, 342, L32
Ehrenfreund, P., Kerkhof, O., Schutte, W. A., et al. 1999, A&A, 350, 240
Fritz, T. K., Gillessen, S., Dodds-Eden, K., et al. 2011, ApJ, 737, 73
Geballe, T. R., & Oka, T. 2010, ApJL, 209, L70
Gerakines, P. A., Whittet, D. C. B., Ehrenfreund, P., et al. 1999, ApJ, 522, 357
Gibb, E. L., Whittet, D. C. B., Boogert, A. C. A., & Tielens, A. G. G. M. 2004, ApJS, 151, 35
Goto, M., Usuda, T., Nagata, T., et al. 2008, ApJ, 688, 306
Hagen, W., Tielens, A. G. G. M., & Greenberg, J. M. 1981, CP, 56, 367
Hasenberger, B., Forbrich, J., Alves, J., et al. 2016, A&A, 593, A7
Hudgins, D. M., Sandford, S. A., Allamandola, L. J., & Tielens, A. G. G. M. 1993, ApJS, 86, 713
Kerkhof, O., Schutte, W. A., & Ehrenfreund, P. 1999, A&A, 346, 990
Kobayashi, N., Tokunaga, A. T., Terada, H., et al. 2000, Proc. SPIE, 4008, 1056
Lucas, P. W., Hoare, M. G., Longmore, A., et al. 2008, MNRAS, 391, 136
Mehringer, D. M., Yusef-Zadeh, F., Palmer, P., & Goss, W. M. 1992, ApJ, 401, 168
Molinari, S., Bally, J., Noriega-Crespo, A., et al. 2011, ApJL, 735, L33
Morales, E. F. E., & Robitaille, T. P. 2017, A&A, 598, A136
Morris, M., & Serabyn, E. 1996, ARA&A, 34, 645
Moultaka, J., Eckart, A., & Mužić, K. 2015, ApJ, 806, 202
Pendleton, Y. J., Sandford, S. A., Allamandola, L. J., Tielens, A. G. G. M., & Sellgren, K. 1994, ApJ, 437, 683
Pontoppidan, K. M., van Dishoeck, E. F., & Dartois, E. 2004, A&A, 426, 925
Ramírez, S. V., Arendt, R. G., Sellgren, K., et al. 2008, ApJS, 175, 147
Rawlings, J. M. C., Williams, D. A., Viti, S., Cecchi-Pestellini, C., & Duley, W. W. 2013, MNRAS, 430, 264
Rayner, J. T., Cushing, M. C., & Vacca, William D. 2009, ApJS, 185, 289
Rayner, J. T., Toomey, D. W., Onaka, P. M., et al. 2003, PASP, 115, 362
Requena-Torres, M. A., Martín-Pintado, J., Martín, S., & Morris, M. R. 2008, ApJ, 672, 352
Requena-Torres, M. A., Martín-Pintado, J., Rodríguez-Franco, A., et al. 2006, A&A, 455, 971
Rodríguez-Fernández, N. J., Martín-Pintado, J., Fuente, A., & Wilson, T. L. 2004, A&A, 427, 217
Sandford, S. A., Allamandola, L. J., Tielens, A. G. G. M., et al. 1991, ApJ, 371, 607
Schultheis, M., Sellgren, K., Ramírez, S., et al. 2009, A&A, 495, 157
Schutte, W. A., Gerakines, P. A., Geballe, T. R., van Dishoeck, E. F., & Greenberg, J. M. 1996, A&A, 309, 633
Shure, M. A., Toomey, D. W., Rayner, J. T., Onaka, P. M., & Denault, A. J. 1994, Proc. SPIE, 2198, 614
Vacca, W. D., Cushing, M. C., & Rayner, J. T. 2003, PASP, 115, 389
van der Tak, F. F. S., van Dishoeck, E. F., & Caselli, P. 2000a, A&A, 361, 327
van der Tak, F. F. S., van Dishoeck, E. F., Evans, N. J., II, & Blake, G. A. 2000b, ApJ, 537, 283
Watanabe, N., Shiraki, T., & Kouchi, A. 2003, ApJL, 588, L121
Yusef-Zadeh, F., Cotton, W., Viti, S., Wardle, M., & Royster, M. 2013, ApJL, 764, L19